



# Applying the geodetic detrending technique for investigating the consistency of GPS L2P(Y) in several receivers

J. M. Juan<sup>1</sup> · J. Sanz<sup>1</sup> · G. González-Casado<sup>1</sup> · A. Rovira-García<sup>1</sup> · C. C. Timoté<sup>1</sup> · R. Orús-Pérez<sup>2</sup>

Received: 31 March 2022 / Accepted: 27 September 2022  
© The Author(s) 2022

## Abstract

Global Navigation Satellite System signals have been used for years to study high-frequency fluctuations ( $f > 0.1$  Hz) in the ionosphere. The customary procedure uses the geometry-free (GF) combination of  $L_1$  and  $L_2$  carriers, for which it is necessary to acquire the  $L_2$  GPS signal. Initially,  $L_2$  had to be acquired from a codeless signal, L2P(Y), using several techniques, some of them requiring the aid of  $L_1$ . New GPS satellites transmit the new  $C_2$  civil code, which can be used to acquire directly  $L_2$ , i.e. L2C. Several publications have reported differences in the GF combination when it is computed from L2P(Y) or L2C. Using two ionospheric scintillation monitoring receivers (ISMRs), these differences were shown to be related to how they acquire  $L_2$ , i.e. if the receiver acquires  $L_2$  with the  $L_1$  aid. However, ISMRs are scarce, so the extension of such a study is not straightforward. The present work uses the geodetic detrending technique to identify whether a conventional geodetic-grade receiver acquires  $L_2$  with the aid of  $L_1$ . The study employs six different receiver types with measurements stored in RINEX formats version 2 and 3. In both formats, we are able to identify if  $L_2$  signal is acquired with  $L_1$  aid. In this way, we show that some receiver types heavily underestimate high-frequency ionospheric fluctuations when using the GF combination. Our results show that the ionosphere-free combination of these carrier phases is not free from high-frequency ionospheric fluctuations, but in some receivers, almost 90% of the high-frequency effects in  $L_1$  remain in such combination.

**Keywords** GNSS signals · Ionosphere · ROTI · Geodetic detrending

## 1 Introduction

Global Navigation Satellite Systems (GNSS) has become a useful tool for ionospheric studies at different spatial and temporal scales. This is thanks to the deployment of networks of ground GNSS receivers worldwide distributed that have been operating continuously for years. Thus, it has been possible to carry out long-term climatological studies with data from such receivers (Olwendo et al. 2016; Watson et al. 2016; Liu et al. 2018).

In particular, the study of high-frequency disturbances of the ionosphere, with periods shorter than tens of seconds (such as ionospheric scintillation), is one of the fields in

which GNSS measurements have been used to characterize the spatial and temporal occurrence of these types of perturbations (Cesaroni et al. 2015; Guo et al. 2017; de Oliveira et al. 2018; Correia et al. 2019; Rovira-García et al. 2020). Since the ionosphere affects GNSS signals, any linear combination of these signals could be used to analyse ionospheric effects, but the most commonly used one is the geometry-free (GF) combination ( $L_{GF}$ ) of carrier phases (Liu et al. 2019), which is defined as:

$$L_{GF} = L_1 - L_2 \quad (1)$$

where  $L_1$  and  $L_2$  are expressed in metres. Indeed, since  $L_1$  and  $L_2$  share the same non-dispersive effects, their difference only accounts for the ionospheric delay (which is mostly proportional to  $f^{-2}$ ) plus a constant term that includes the difference of the carrier phase ambiguity of each signal (Sanz et al. 2013). In fact,  $L_{GF}$  could be understood as the  $L_1$  signal detrended from the non-dispersive effects by subtracting  $L_2$ . Therefore, during a continuous arc of carrier phase measurements gathered by a receiver (rcv) from a satellite (sat), the

✉ J. M. Juan  
jose.miguel.juan@upc.edu

<sup>1</sup> Research Group of Astronomy and Geomatics (gAGE),  
Universitat Politècnica de Catalunya (UPC), Jordi Girona,  
1-3, 08034 Barcelona, Spain

<sup>2</sup> Wave Interaction and Propagation Section, European Space  
Agency (ESA), Noordwijk, The Netherlands

temporal rate of change of  $L_{GF}$  is proportional to the rate of change in the total electron content (ROT) affecting the GNSS signals:

$$\text{ROT}_{\text{rcv}}^{\text{sat}} = \alpha_{\text{GF}} \cdot \frac{\Delta L_{\text{GFrcv}}^{\text{sat}}}{\Delta t} \quad (2)$$

where  $\alpha_{\text{GF}}$  is a factor to convert the  $L_{GF}$  units (m) into Total Electron Content Units (TECU) ( $1 \text{ TECU} = 10^{16} \text{e}^- / \text{m}^2$ ), which is a unit linked to the ionosphere (in particular, for GPS frequencies  $f_1$  and  $f_2$ ,  $\alpha_{\text{GF}} = 9.52 \text{ TECU/m}$ ) and  $\Delta t$  is the sampling interval of the measurements, typically 30 s or 1 s. Therefore, using ROT, for each satellite-receiver pair, it is possible to define the index ROTI as the standard deviation of ROT (Pi et al. 1997) over a time interval, typically 5 min or 1 min, depending on  $\Delta t$ .

Due to its simplicity, ROTI has become a common metric to measure high-frequency disturbances in the ionosphere (Zakharenkova and Astafyeva 2015; Yang and Liu 2016; Cherniak et al. 2018; Liu et al. 2019; Zhao et al. 2022). However, the use of ROTI presents some drawbacks linked to the use of two signals. On the one hand, the proportionality of the ionospheric delays in  $L_1$  and  $L_2$  is broken when the GNSS signals experience diffraction, which are typically experienced at low latitudes, i.e. for large amplitude scintillation values (Carrano et al. 2019). Under those circumstances, ROT would measure an intermediate value for the high-frequency ionospheric effects between those of  $L_1$  and  $L_2$ . On the other hand, since 2005, new GPS satellites (blocks IIR-M and II-F) are transmitting a new  $L_2$  civil signal (Leveson 2006), being this new signal (L2C in RINEX-v3 notation) acquirable directly, in the same manner as the civil signal in  $L_1$  (L1C). Therefore, with the new L2C signal, one can build  $L_{GF}$  by means of (1) from two independent signals. However, this is not the case for the older GPS blocks, where  $L_2$  must be acquired from a codeless signal, L2P(Y) or L2W according to the RINEX-v3 notation. In this regard, there are several techniques that can be used for such acquiring purpose (Woo 1999). These L2W acquisition processes reduce the power of the signal and present more abundant cycle slips than  $L_1$  (Juan et al. 2017).

Furthermore, some of the L2W acquisition techniques use  $L_1$  (i.e.  $L_1$ -aided), and therefore L2W is not completely independent of  $L_1$ , so high-frequency ionospheric effects in  $L_1$  will affect in a similar way to L2W and, consequently, to the resulting  $L_{GF}$  value (McCaffrey et al. 2018). Therefore, as it was reported in Yang and Liu (2017), the comparison of ROTIs of two collocated receivers yields inconsistent values of ROTI depending on the procedure used by each receiver to obtain  $L_2$ .

Measuring scintillation with GNSS requires to isolate the high-frequency fluctuations of the ionospheric delay experienced by the GNSS signal. This isolation can be done by

applying a high pass filter (HPF), such as a sixth-order Butterworth filter (Van Dierendonck et al. 1993), with a typical cut-off frequency of 0.1 Hz. However, other effects such as cycle slips in the carrier phase measurements or receiver clock jitter can still be present after the HPF and should be removed or mitigated before the HPF. There are several ways/techniques to do this, for instance, to use open-loop receivers (Linty and Dovis 2019), to gather data at high frequency (50 Hz), or to synchronize the receiver clock with a very stable clock. Ionospheric Scintillation Monitoring receivers (ISMR) are receivers that apply some of these techniques and, consequently, are able to monitor directly the high-frequency fluctuations of the ionospheric effects in any of the GNSS signals.

Applying a sixth-order Butterworth filter over data gathered at 50 Hz by a Septentrio PolaRxS Pro receiver and by a Trimble NetR9 receiver, McCaffrey et al. (2018) showed that, for the Septentrio receiver, the residuals of L2C were greater than those of L2W. They justified the lower residuals for L2W by the way L2W is obtained in a Septentrio receiver (with the  $L_1$  aid). However, in the case of the Trimble receiver, the L2W and L2C residuals were quite similar, in line with the results in Yang and Liu (2017), which, jointly with other experiments, allowed McCaffrey et al. (2018) to conclude that Trimble receivers used  $L_1$  to acquire, not only L2W, but also L2C.

ISMRs are quite scarce, so it is difficult to extend the study done in McCaffrey et al. (2018), not only to other receiver types but also to years in which high-rate data is stored in RINEX v2 format, which does not specify what type of  $L_2$  signal attribute it contains. In this regard, Juan et al. (2017) and Nguyen et al. (2019) presented the geodetic detrending (GD). The GD technique consists on an accurate modelling of the non-dispersive (geodetic) effects of the GNSS signals, including the receiver clock fluctuations, which also allowed the identification of cycle slips that are usually present in the measurements of conventional receivers under scintillation conditions. In this way, the use of GD allows the isolation of the ionospheric delays, including the high-frequency ones, in a manner equivalent to the ISMRs. Once the ionospheric delays are isolated, the high-frequency modes can be enhanced (i.e. isolated) using an HPF or ROT and its standard deviation ( $\sigma_\phi$  or ROTI). In the present work, we used HPF, but similar conclusions can be extracted by using the ROT.

The use of the GD allows the extension of the study carried out in McCaffrey et al. (2018), but, in our case, with conventional receivers working at 1 Hz. This is applied not only to recent measurements where, thanks to the RINEX v3 format, it is possible to distinguish between L2C and L2W measurements but also to older measurements written in RINEX v2 format, where the carrier phase is written without attribute.

The remaining of the paper is organized as follows. In Sect. 2, we explain the methodology used to determine if specific L2W measurements are acquired with the  $L_1$  aid. In Sect. 3, we present the data used for the experiment, including the ionospheric conditions when these data were collected. In Sect. 4, we present the results separated into two subsections, depending on the way the data was stored (RINEX v2 or RINEX v3 format). Finally, in Sect. 5, we present our conclusions.

## 2 Methodology

As mentioned in the introduction, in order to apply the GD to any GNSS signal, all model terms on the carrier phase measurements must be considered up to the centimetre level or better. For instance, for a receiver (rcv) and a satellite (sat), the carrier phase measurement  $L_1$ , can be modelled as:

$$L_{1\text{rcv}}^{\text{sat}} = \rho_{\text{rcv}}^{\text{sat}} + c \cdot (T_{\text{rcv}} - T^{\text{sat}}) + M_{\text{rcv}}^{\text{sat}} \cdot \text{Trop}_{\text{rcv}} + \lambda_1 \cdot (N_{1\text{rcv}}^{\text{sat}} + \delta_{\text{rcv}} + \delta^{\text{sat}}) - \alpha_1 \cdot I_{\text{rcv}}^{\text{sat}} \tag{3}$$

where  $\rho$  is the Euclidean distance between the sat and rcv antenna phase centres,  $c$  is the speed of light in the vacuum,  $T_{\text{rcv}}$  and  $T^{\text{sat}}$  are the receiver clock and satellite clock offsets with respect to GPS time,  $\text{Trop}_{\text{rcv}}$  is the zenith tropospheric delay at the receiver position,  $M_{\text{rcv}}^{\text{sat}}$  is an obliquity factor which depends on the elevation,  $\lambda_1$  is the wavelength of the  $L_1$  signal,  $(N_{1\text{rcv}}^{\text{sat}} + \delta_{\text{rcv}} + \delta^{\text{sat}})$  is the carrier phase ambiguity that can be split into an integer part  $N_{1\text{rcv}}^{\text{sat}}$  plus two real-valued instrumental delays  $\delta$ ,  $I_{\text{rcv}}^{\text{sat}}$  is the ionospheric delay, in TECU, experienced by the signal, and  $\alpha_1$  is a factor which converts the ionospheric delay, in TECU, to metres of  $L_1$ .

Since the non-dispersive parameters can be known or estimated accurately, it is possible to compute the GD of  $L_1$ , denoted as  $\tilde{L}_1$ , by subtracting such parameters from the measurement, through:

$$\tilde{L}_{1\text{rcv}}^{\text{sat}} = L_{1\text{rcv}}^{\text{sat}} - [\rho_{\text{rcv}}^{\text{sat}} + c \cdot (T_{\text{rcv}} - T^{\text{sat}}) + M \cdot \text{Trop}_{\text{rcv}}] = -\alpha_1 \cdot I_{\text{rcv}}^{\text{sat}} + \lambda_1 \cdot (N_{1\text{rcv}}^{\text{sat}} + \delta_{\text{rcv}} + \delta^{\text{sat}}) \tag{4}$$

In this work, we have used the precise products of the International GNSS Service (IGS) server (in <https://gdc.cddis.eosdis.nasa.gov/gps/products/>) for troposphere and satellite orbit and clock corrections, while the receiver clock corrections were computed following the methodology described in Juan et al. (2017). It is worth to note that a detrending similar to (4) can be applied to any carrier phase measurement at other frequency.

After the GD computation in (4), a HPF can be applied to obtain the high-frequency effects of the ionospheric delay on  $L_1$ ,  $\text{HPF}(\tilde{L}_1)$ . Furthermore, the standard deviation of these residuals during 60 s ( $\sigma_\phi$ ) can be calculated, which is equivalent to the  $\sigma_\phi$  provided by an ISMR receiver as shown by Nguyen et al. (2019).

In any case, by means of an HPF or ROT, high-frequency ionospheric effects can be isolated (i.e. enhanced) in any GNSS signal and, similar to McCaffrey et al. (2018), these effects can be compared between different frequencies and combination of frequencies. Ideally, if  $L_2$  is obtained directly without the aid of  $L_1$  (as in the case of L2C) and in the presence of refractive scintillation, which is the typical case for scintillation experienced at high latitude, the next relationship is expected:

$$\text{HPF}(\tilde{L}_{2\text{rcv}}^{\text{sat}}) = \frac{f_1^2}{f_2^2} \cdot \text{HPF}(\tilde{L}_{1\text{rcv}}^{\text{sat}}) = 1.65 \cdot \text{HPF}(\tilde{L}_{1\text{rcv}}^{\text{sat}}) \tag{5}$$

And, for the GF and the ionosphere free (IF) combinations, omitting the references to satellite (sat) and receiver (rcv) to simplify the expressions, the following relationships are expected:

$$\begin{aligned} \text{HPF}(\tilde{L}_{\text{GF}}) &= \text{HPF}(\tilde{L}_1 - \tilde{L}_2) = \left(1 - \frac{f_1^2}{f_2^2}\right) \cdot \text{HPF}(\tilde{L}_1) \\ &= -0.65 \cdot \text{HPF}(\tilde{L}_1) \\ \text{HPF}(\tilde{L}_{\text{IF}}) &= \frac{f_1^2 \cdot \text{HPF}(\tilde{L}_1) - f_2^2 \cdot \text{HPF}(\tilde{L}_2)}{f_1^2 - f_2^2} = 0 \end{aligned} \tag{6}$$

Therefore, any significant deviation of the actual relationship between residuals, with respect to those theoretical expectations, would reflect an anomalous  $L_2$  measurement generation. Taking this into account, in the present work we compute the relationship between HPF residuals following the next steps:

1. Using the GD technique, we calculate the HPF residuals for  $L_1$ ,  $L_2$ ,  $L_{\text{GF}}$ , and  $L_{\text{IF}}$ . For brevity, we refer to these residuals as  $\text{HPF}(L_1)$ ,  $\text{HPF}(L_2)$ , ..., i.e. assuming GD has been performed and omitting rcv and sat.
2. For any pair of receiver and satellite, the standard deviation of  $\text{HPF}(L_1)$  during 1 min is calculated, i.e.  $\sigma_\phi$ . Arcs of carrier phase measurements are selected when during any continuous 1-min interval it is found a value  $\sigma_\phi > 0.2$ , being the elevation angle above 40 deg. In this way, we consider only arcs with some scintillation activity not linked to low elevation.

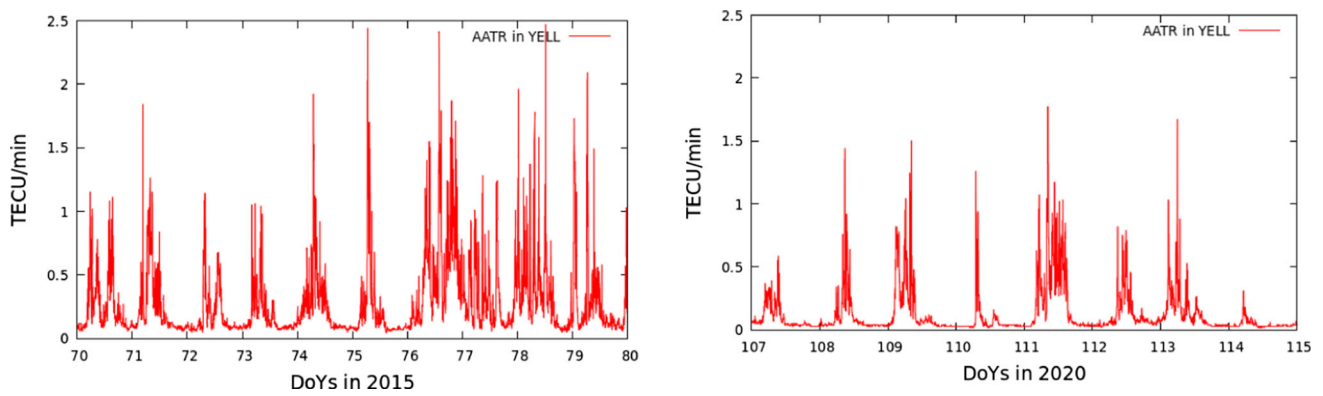


**Fig. 1** AATR values at station yell in Canada, around the St. Patrick storm in 2015 076 (left) and during 2020 DoYs 107–114 (right)

**Fig. 2** Map with the high latitude receivers used in the experiment

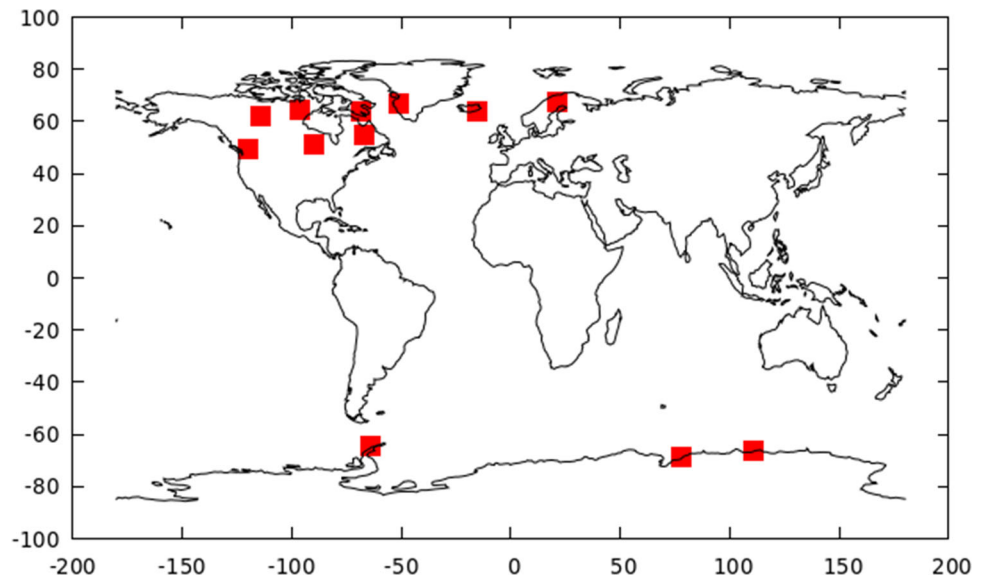


**Table 1** List of the 13 high latitude receivers used in the study

Station	Receiver type	Lon. (°)	Lat. (°)	Year and DoY
cas1	TRIMBLE_NETR9	110.5	− 66.1	2015 076
dav1	LEICA_GRX1200GGP	78.0	− 68.4	2015 076
drao	TRIMBLE_NETR9	− 119.6	49.1	2015 076
hofn	LEICA_GR25	− 15.2	64.1	2015 076
kely	ASHTECH_UZ-12	− 50.9	66.8	2015 076
kiru	SEPT_POLARX4	21.0	67.7	2015 076
palm	ASHTECH_UZ-12	− 64.1	− 64.6	2015 076
yell	JAVAD_TRE_3N_DEL	− 114.5	62.3	2015 076
				2020 111
bake	TPS_NET-G3A	− 96.0	64.2	2020 111
iqal	TPS_NET-G3A	− 68.5	63.6	2020 111
pic1	SEPT_POLARX5	− 90.2	51.3	2020 111
sch2	JAVAD_TRE_3N_DEL	− 66.8	54.7	2020 111
yel2	SEPT_POLARX5TR	− 114.5	62.3	2020 111

3. Finally, considering only the arcs selected in the previous point, we have fitted, through a linear model, the relationship of  $HPF(L_1)$  with  $HPF(L_2)$ ,  $HPF(L_{GF})$ , or  $HPF(L_{IF})$ , where the slope of this lineal model is considered as the actual relationship. The fitting coefficients are compared with (5) and (6). To this end, we have excluded data with  $\sigma_\phi > 0.1$  for the fitting, since they could be close to the noise level of the GD, diminishing the ratio between residuals.

### 3 Data set

To analyse the HPF residuals, we have used two days with high ionospheric activity: day of the year (DoY) 111 in 2020 and DoY 076 in 2015. The along arc TEC rate (AATR) values (Juan et al. 2018a) for the station yell (located in Canada) are depicted in Fig. 1.

Although 2020 is close to the solar minimum, DoY 111 presented high ionospheric activity at high latitudes, as reflected in Fig. 1 (right panel). In addition, during this day most of the high-rate data files in the IGS network are stored in RINEX v3 format, making possible to collect L2W and L2C measurements from many stations.

However, during DoY 111 in 2020, at high latitudes, almost all the stations were equipped with one of three types of receivers: Septentrio, Javad, or TPS (Topcon). Therefore, if one wants to analyse other receiver types under high ionospheric activity, one needs to process older data, when more types of receivers worked at 1 Hz. In this regard, DoY 076 in 2015 was one of the most active days (St. Patrick storm) during the last Solar Cycle. This is reflected in the corresponding AATR values depicted in Fig. 1 (left panel). However, unlike in 2020, few receivers provided data in RINEX-v3 format, so we have used data in RINEX-v2 format where the attribute of  $L_2$  is not written. In this sense, apart from analysing more types of receivers, we have the opportunity to demonstrate that the methodology is capable of distinguishing whether the  $L_2$  data have been acquired through its correlation with  $L_1$ .

For the study, we have selected a list of 13 high-latitude receivers, where diffractive scintillation is not expected. These receivers are depicted in the map in Fig. 2. Moreover, Table 1 shows, in addition to the location of each receiver, the receiver types and the days for which we have used their data: 2020 111 for data in RINEX-v3 format, and 2015 076 for data in RINEX-v2 format. As it can be seen, we have selected, for each type of receiver, two stations in order to achieve some redundancy in the results. Moreover, two collocated receivers of a different type, *yell* and *yel2*, have been considered.

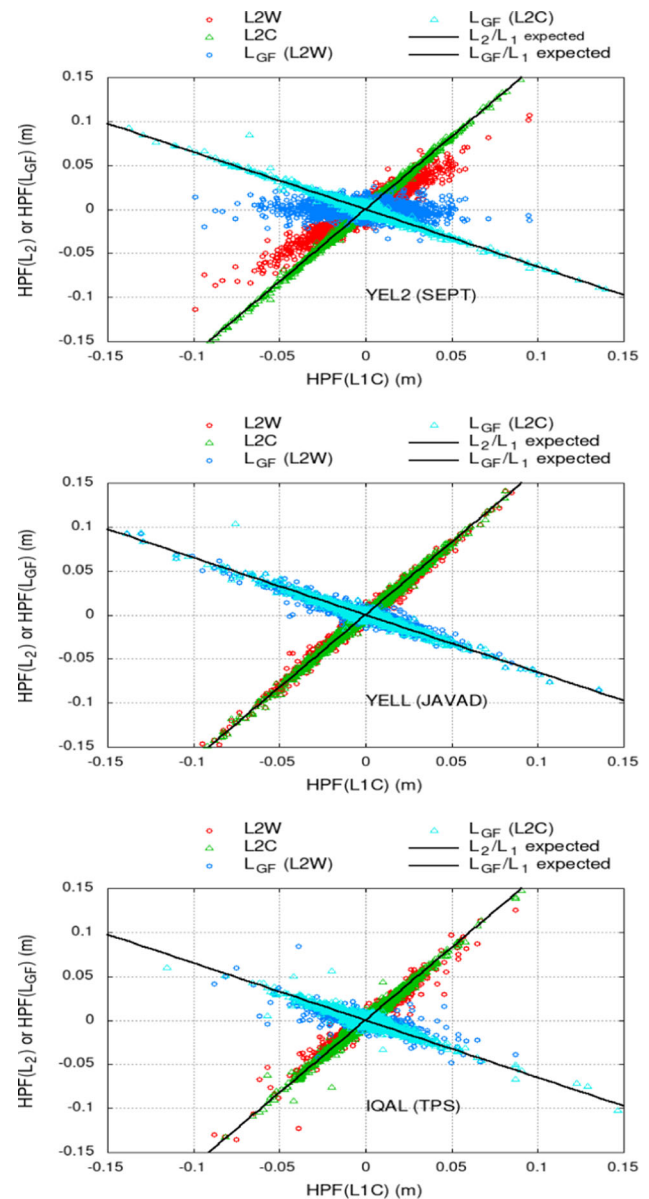


**Fig. 3** Scatter plots between residuals from  $HPF(L1C)$  and:  $HPF(L2C)$  (green),  $HPF(L2W)$  (red),  $HPF(L_{GF})$  with  $L2C$  (cyan) and  $HPF(L_{GF})$  with  $L2W$  (blue). Straight lines represent the expected relationships between  $L_2$  and  $L_1$  residuals (1.65) and between  $L_{GF}$  and  $L_1$  residuals ( $-0.65$ ). The comparison is done for three different types of receivers: *yel2* (Septentrio, top), *yell* (Javad, middle) and *iqal* (TPS, bottom)

## 4 Results

### 4.1 HPF residuals in 2020 111 (RINEX-v3 format)

Once we compute the HPF residuals for the different signals included in the data files in RINEX-v3 format, we can proceed to analyse the relationships between them. Figure 3 depicts the scatter plots referring to the HPF residuals of  $L_1$  for three stations: *yel2*, in the top panel, *yell* in the central panel and *iqal* in the bottom panel. As it can be seen from



**Table 2** Ratios of HPF( $L_2$ ), HPF( $L_{GF}$ ) and HPF( $L_{IF}$ ) with respect to HPF( $L_{1C}$ ), taking into account how  $L_2$  is obtained (i.e. using L2W or L2C)

STA	REC	#L2W/#L2C	L2W	L2C	$L_{GF}$ (L2W)	$L_{GF}$ (L2C)	$L_{IF}$ (L2W)	$L_{IF}$ (L2C)
Expected			1.65		-0.65		0.00	
pic1	SEPT	306/188	1.06	1.62	-0.06	-0.62	0.91	0.04
yel2	SEPT	3797/3247	1.08	1.65	-0.08	-0.65	0.87	0.00
bake	TPS	1482/933	1.37	1.60	-0.37	-0.60	0.43	0.07
iqal	TPS	1993/1627	1.47	1.62	-0.47	-0.62	0.27	0.05
sch2	JAVAD	1401/991	1.64	1.65	-0.64	-0.65	0.01	0.00
yell	JAVAD	4557/3004	1.61	1.63	-0.61	-0.63	0.06	0.02

Table 1, these three stations are equipped with three different types of receivers. In each panel of Fig. 3, the different HPFs are represented against the HPF( $L_{1C}$ ): the HPF(L2W), in red; the HPF(L2C) in green; the HPF( $L_{GF}$ ) when  $L_{GF}$  is computed using L2W, in blue; and, finally, the HPF( $L_{GF}$ ) when it is computed through the L2C, in cyan. In addition to the scatter plots, two straight dashed lines are included in each panel showing the expected relationships of  $L_1$  with  $L_2$  (1.65) and with  $L_{GF}$  (-0.65), since HPF residuals are in metres.

Figure 3 depicts that receivers Javad (*yell*) and TPS (*iqal*) exhibit the expected relationships between the different HPF residuals. However, Septentrio (*yel2*) only presents the correct relationship for L2C or for  $L_{GF}$ , when the combination is obtained using L2C. For L2W or for  $L_{GF}$  using L2W, the relationship is far from what it is expected. This observation implies that, for instance, the high-frequency values of  $L_{GF}$  are clearly lower if the combination is calculated using L2W if compared when the combination is calculated with L2C. This result obtained for the Septentrio receiver agrees with the work of McCaffrey et al. (2018).

A more quantitative comparison can be made if we calculate the parameters of a linear fit for the ratios between HPF( $L_{1C}$ ) and HPF(L2C), HPF(L2W), HPF( $L_{GF}$ ), and HPF( $L_{IF}$ ). Table 2 shows such relationships, where the second row represents the expected relationship between HPF( $L_{1C}$ ) and the rest of the signals or combinations (these expected relationships are shown as the dashed lines in Fig. 3). The third column of Table 2 shows the number of data used for each L2C and L2W fit, according to the criteria explained in the data section. As it can be seen in the two rightmost columns, we have also included the relationships with the  $L_{IF}$  combination. For clarity purposes, these relationships were not represented in the scatter plots of Fig. 3.

As we discussed in the methodology section, once we know the relationship between  $L_2$  and  $L_1$ , we can derive the relationships for the combinations in Table 2. For instance, if  $\beta$  is the ratio between  $L_2$  and  $L_1$  residuals, according to (4), the relationship between  $L_{GF}$  and  $L_1$  should be  $1-\beta$ , and between  $L_{IF}$  and  $L_1$  should be  $(1.65-\beta)/0.65$ . However, we

have preferred to keep the corresponding columns since  $L_{GF}$  and  $L_{IF}$  are the combinations used for ionospheric studies and for navigation, respectively. Therefore, it is important to show directly how the high-frequency ionospheric effects in  $L_1$  affect these combinations.

Looking at Table 2, it can be seen that either using L2C directly or building any combination ( $L_{GF}$  or  $L_{IF}$ ), the ratios of their HPF residuals to the L1C ones (columns 5, 7, and 9) are close to those expected, with a correlation coefficient close to 1. McCaffrey et al. (2018) showed that L2C in a Septentrio receiver is acquired without the aid of L1C, and based on the results of Yang and Liu (2017), they suggested that Javad receivers appear to use L1C to acquire L2C. Our results suggest that the three types of receivers, including Javad, acquire L2C without the aid of L1C.

In the case of L2W, in spite of the three fittings having a high correlation coefficient ( $> 0.97$ ), it is clear that only the Javad receiver seems to acquire the signal without L1C aiding. The L2W acquired by the Septentrio receiver is more affected by the L1C-aid than the TPS receiver.

This anomalous measurement of L2W is responsible for an underestimation of the high-frequency fluctuations in the  $L_{GF}$  combination (clearly reduced in the Septentrio receiver). It is also shown that for the  $L_{IF}$  combination, the high-frequency fluctuations are clearly present (for a Septentrio receiver, around 90% of the residuals in L1C are present in the  $L_{IF}$  residuals). However, it is worth saying that this only occurs for high-frequency data, i.e. with a sampling interval smaller than 10 s. For a larger sampling, for instance 30 s, the effects are not as large.

A detailed study of how the results in Table 2 affect the high-frequency ionospheric measurements is shown in Fig. 4. The example corresponds to the measurements of three different receivers from Table 2, measuring data from GPS satellite G31.

The left-hand panels of Fig. 4 depict the HPF ionospheric residual for the receivers Septentrio (*yel2*), Javad (*yell*) and TPS (*iqal*). At the left-hand panels, the residuals of L1C (in metres) are depicted in the bottom plots, while in the middle

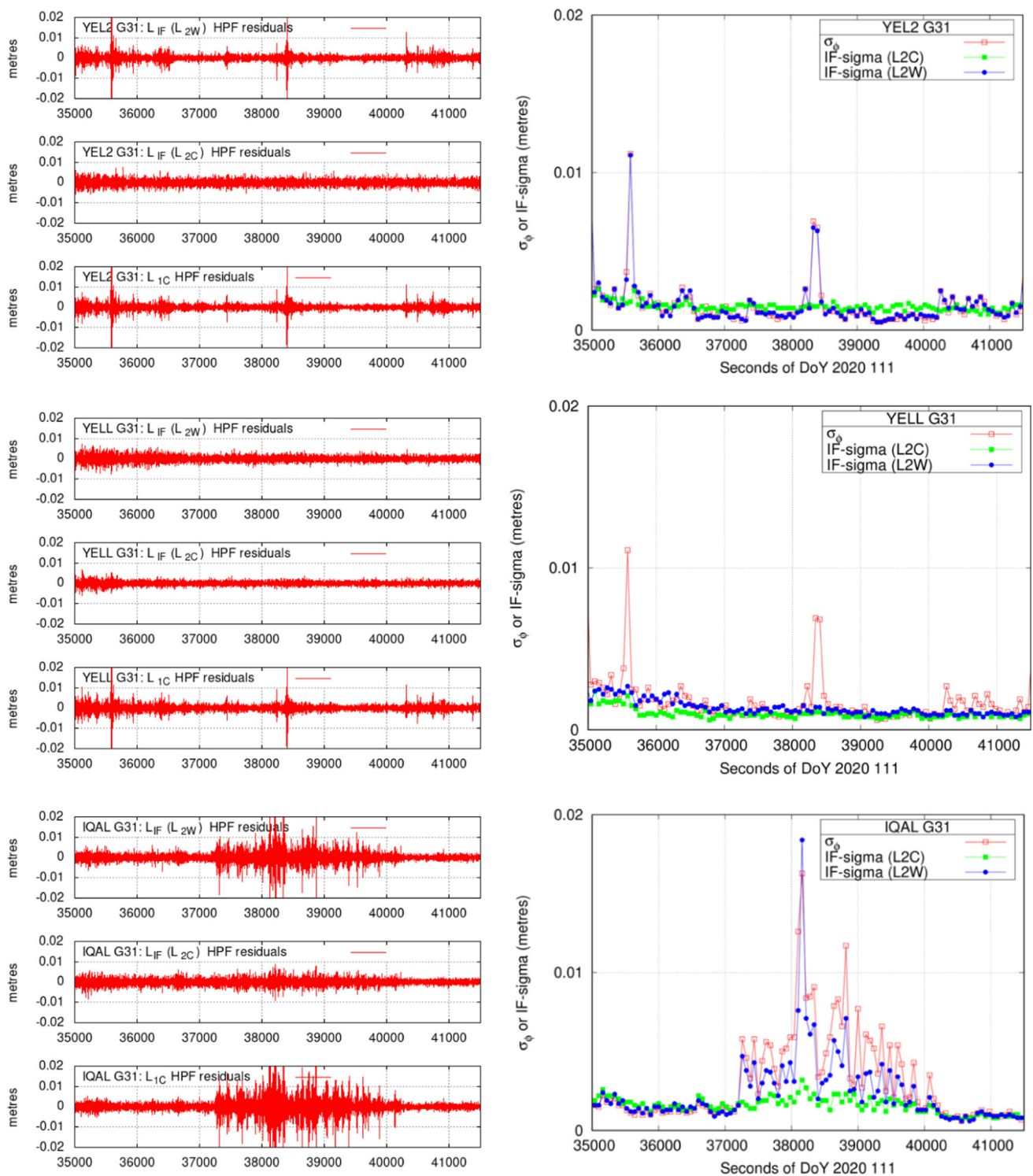


**Fig. 4** Example of how the high-frequency fluctuations in ionospheric residuals affect to different signals for a receiver Septentrio (yel2, top row), Javad (yell, middle row), and TPS (iqal, bottom row). The measurements correspond to satellite G31 during DoY 111 in 2020. Each panel at the left column shows the HPF residual of L<sub>1C</sub> (bottom plot),

the HPF residuals of the L<sub>IF</sub> computed with L2C (middle plot), and the HPF residuals of the L<sub>IF</sub> computed with L2W (top plot). The plots at the right column depict the  $\sigma_\phi$  of L<sub>1</sub>, in red, the IF-sigma for L<sub>IF</sub> computed with L2W (in blue), and the IF-sigma of the L<sub>IF</sub> computed with L2C (in green)

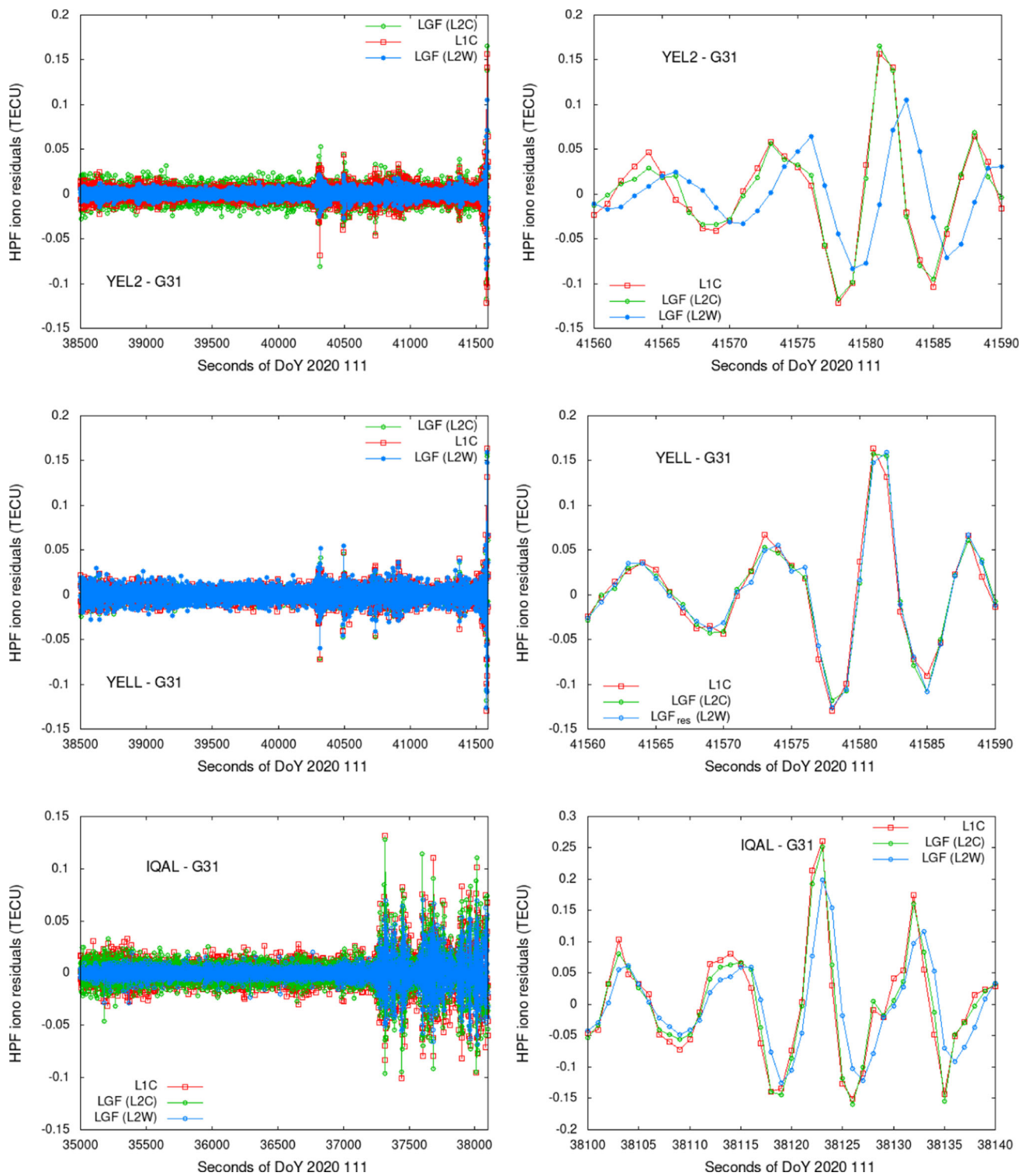


**Fig. 5** HPF residuals for GPS satellite G31, from a Septentrio receiver (yel2, top row), Javad (yell, middle row), and TPS (iqal, bottom row). The left column depicts the HPF residuals of L1C in red, the  $L_{GF}$  HPF

residuals computed with L2W in blue, and the  $L_{GF}$  HPF residuals computed with L2C in green. The plots at the right column are a zoomed view of its correspondent left column plots



and top plots are depicted the HPF residuals of  $L_{IF}$ , when they are calculated using L2C or using L2W, respectively.

As it can be seen, except for station *yell* (Javad), and due to the way the other receivers acquire L2W, most of the high-frequency fluctuations in L1C are visible in  $L_{IF}$ , when L2W is used, and this ionosphere-free combination is not really ionosphere-free for high-frequency variations of the ionospheric delay. This is in full agreement with the results shown in Table 2.

Since  $L_{IF}$  is a usual combination used for precise positioning, as shown in Juan et al. (2018b), the high-frequency fluctuations will produce a noisier behaviour of  $L_{IF}$ , degrading the positioning performance. The HPF residuals of the  $L_{IF}$  can be seen in the plots located at the right column of Fig. 4, where  $\sigma_\phi$  of L1C (in metres) is depicted together with the IF-sigma parameter, defined in Juan et al. (2017) as the 1-min standard deviation of the HPF residuals of the  $L_{IF}$ . One can see that for the Septentrio and the TPS receivers, the IF-sigma values of  $L_{IF}$  are not too far from the  $\sigma_\phi$  values of L1C when  $L_{IF}$  is calculated using L2W. In contrast, for the Javad receiver (i.e. when the  $L_{IF}$  combination uses L2C) the  $L_{IF}$  combination is free from these high-frequency fluctuations in the ionosphere.

Figure 5 depicts for the same measurements shown in the previous Fig. 4, the effects in  $L_{GF}$  of the high-frequency ionospheric fluctuations. To facilitate an easier comparison, residuals are plotted in TECU (which corresponds to 0.162 m in  $L_1$ , and 0.105 m in  $L_{GF}$ ). According to Table 2, an underestimation of the high-frequency ionospheric residuals should be expected when they are calculated using  $L_{GF}$  from  $L_1$ -aided L2W (Septentrio or TPS receiver) with respect to the ones computed using  $L_1$ . This is confirmed in the top and bottom plots located in the left column of Fig. 5, where the ionospheric delays using  $L_{GF}$  from L2W (blue points) are clearly smaller than the ionospheric delays in  $L_1$  (red points) or in  $L_{GF}$  using L2C (green points). However, this is not produced by a smaller noise in the estimation of the ionospheric delay but rather by an underestimation of the value, linked to the way L2W is acquired. On the contrary, in the Javad receiver, or for the other receivers, when  $L_{GF}$  is calculated using L2C, the residuals are quite equivalent and a noisier behaviour is only observed in the results with L2C for the receiver Septentrio. These results agree with those in Yang and Liu (2017), despite the fact that their study was carried out with low-latitude stations. They found for the Septentrio receiver clearly higher ROTI values when  $L_{GF}$  was calculated using L2C than the ROTI values obtained using L2W, while, for the Javad receiver, the ROTI values with L2C and L2W were quite similar.

Finally, the plots at the right column of Fig. 5 show that the technique used to acquire L2W not only affects to the  $L_{GF}$  values but also can produce delays in the HPF residuals. Indeed, these panels correspond to a shorter time window,

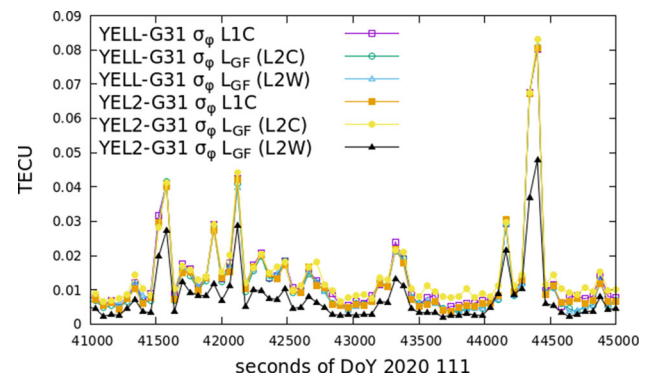


**Fig. 6**  $\sigma_\phi$  of the high-frequency ionospheric fluctuations, for satellite G31 and the collocated receivers *yel2* (Septentrio) and *yell* (Javad), using different measurements: L1C,  $L_{GF}$  with L2C and  $L_{GF}$  with L2W

with respect to the plots in the left column of Fig. 5, where it can be seen that, for the receiver Septentrio (*yel2*) and TPS (*iqal*), and when  $L_{GF}$  is calculated using L2W, the residuals are delayed with respect to the residuals of L1C, or  $L_{GF}$  using L2C. On the contrary, for Javad (*yell*), the three residuals are synchronized.

One of the most relevant findings in Yang and Liu (2017) was the inconsistent ROTI values in collocated receivers which evidenced the appropriateness of comparing ROTI values obtained from different receivers. Since Septentrio (*yel2*) and Javad (*yell*) are collocated receivers, we can compare the high-frequency ionospheric residuals obtained from L1C and  $L_{GF}$  (with L2W or L2C). This is presented in Fig. 6, where the 1-min standard deviation of the residuals,  $\sigma_\phi$ , is plotted in TECU instead of metres or radians to ease the comparison. As it can be seen, for the six-time series of  $\sigma_\phi$  values, only the values for  $L_{GF}$  calculated with L2W and measured by the receiver Septentrio (*yel2*) are inconsistent (underestimated) with respect to the other five measurements. Therefore, the inconsistency reported in Yang et al. (2017) occurs in those receivers acquiring L2W with  $L_1$  aid.

Furthermore, notice that Septentrio (*yel2*) tracks L2C(L), or L2L in RINEX-v3 notation, while Javad (*yell*) tracks L2C(M + L), or L2X in RINEX-v3 notation. Since the two signals present consistent results in L2C, one can conclude that the inconsistency is not in the L2C tracking, as it is suggested in Yang and Liu (2017), but in the L2W acquisition.

#### 4.2 HPF residuals in 2015 076 (RINEX-v2 format)

In this section, we show that the analysis performed using data stored in RINEX-v3 format can also be done for data stored in RINEX-v2 format (the usual format in the past) and, therefore, we can extend the study to other receivers which stored data in this format. As it is known, the problem with RINEX-v2 format is that only the carrier phase frequency

**Table 3** Ratio of high-frequency residuals between  $L_2$  and  $L_1$  during DoY 2015 076

STA	REC	# obs $P_2$ /#obs $C_2$	$L_2$ ( $P_2$ )	$L_2$ ( $C_2$ )	STA	REC	# obs $P_2$ /#obs $C_2$	$L_2$ ( $P_2$ )	$L_2$ ( $C_2$ )
kiru	SEPT	12,915/9337	1.51 (1.10)	1.63	cas1	TRIMBLE	13,180/10,597	1.31	1.34
yell	JAVAD	20,638/0	1.61	–	drao	TRIMBLE	473/336	1.24	1.24
kely	ASHTECH	5117/0	1.53	–	dav1	LEICA GRX1	7917/0	1.16	–
palm	ASHTECH	2257/0	1.62	–	hofn	LEICA GR25	3644/0	1.15	–

label (i.e.  $L_1$  or  $L_2$ ) is written without specifying the signal attribute (i.e. L1C, L2C, L2W).

The list of receivers used for this study is presented in Table 1, where we have included two receivers, Septentrio (*kiru*) and Javad (*yell*), with receiver types studied in the previous section, just for confirming the results when we use data in RINEX-v2 format. The ratio between the  $L_2$  and  $L_1$  HPF residuals obtained from this new set of receivers is presented in Table 3 which is slightly different from Table 2. For instance, since the ratios for  $L_{GF}$  and  $L_{IF}$  can be easily calculated from the ratios between  $L_2$  and  $L_1$ , we have only written these latter ratios. Also, since only the code types are specified in RINEX-v2 ( $P_2$  or  $C_2$  in the header file), unlike Table 2, the third column refers to the number of measurements having  $C_2$  and the number of measurements having  $P_2$  (i.e. all the measurements). Consequently, the fourth column corresponds to  $L_2$  when  $P_2$  is present and the fifth column corresponds to  $L_2$  when  $C_2$  is present.

Moreover, there are some features that are not shared by all the receivers. For instance, only Septentrio and Trimble receivers were collecting  $C_2$  during the day of the experiment. In this sense, we have assumed that receivers without  $C_2$  are measuring L2W. Station *cas1*, collected  $C_2$  data or  $P_2$  data, but not both at the same time, while receiver *drao* (which, as *cas1*, have a Trimble receiver) collects both codes when possible (from GPS blocks IIR-M and IIF).

Furthermore, in Fig. 7, three examples are depicted illustrating the delays of the HPF residuals of the  $L_{GF}$  combination with respect to the  $L_1$  residuals. The examples are for the three receiver types not studied in the previous section: *kely* (Ashtech) in the left panel, *drao* (Trimble) in the middle panel and *dav1* (Leica) in the right panel.

Looking at Table 3, the results for *yell* receiver (Javad) are similar to the ones in the previous section. Hence, assuming that the receiver is measuring L2W, it can be concluded that it is not obtained with the  $L_1$  aid.

In the case of *kiru* (Septentrio) the results for  $L_2$ , when  $C_2$  is present, are in line with the results for L2C for a Septentrio receiver shown in the previous section. The ratio for  $L_2$  when  $P_2$  is present (i.e. all the measurements) is clearly larger than the ratio for L2W shown in the previous section. However, if we calculate the ratio only for the measurements without  $C_2$  (GPS old blocks) we obtain a smaller value (shown in

parenthesis) that is compatible with the value for L2W in the previous section. Thus, it can be concluded that the Septentrio receiver records L2C when  $C_2$  is present and L2W when  $C_2$  is not present. In fact, this can be verified in a much simpler way, since for some stations the same data can be found stored in RINEX-v2 and RINEX-v3 formats.

For Ashtech receivers the ratio between L2W and L1C is close to the expected one, so it can be concluded that the acquisition method for L2W, Z-tracking, does not affect the  $L_2$  value as much. However, in Fig. 7 a small delay of LGF residuals can be seen with respect to those of  $L_1$ , which means that L2W is acquired with  $L_1$  aid.

Trimble receivers present a ratio far from expected, even when  $C_2$  is present. In fact, both ratios are very similar. Therefore, it can be concluded that they acquire  $L_2$  with the  $L_1$  aid, even when  $C_2$  is present. Considering that in Yang and Liu (2017) no significant differences were found when ROTI was calculated using L2C or L2W, one can conclude that Trimble receivers use  $L_1$  aid to acquire L2W and L2C, which is in full agreement with the results of McCaffrey et al. (2018). This is also confirmed in Fig. 7, checking the results for *drao* receiver.

For Leica receivers, which only collected L2W, it is evident that the ratio is far from the expected one, meaning that they acquire L2W with  $L_1$  aid, which is also confirmed in Fig. 7.

Finally, we have to point out that the specific firmware of a receiver does not affect the behaviour observed in its HPF residuals, since the same behaviour has been found with the same type of receiver from data collected in 2015 and in 2020, with different firmware.

## 5 Conclusions

The present work shows that the Geodetic Detrending over GNSS data collected at 1 Hz is a useful tool to analyse the effects of high-frequency (i.e. larger than 0.1 Hz) ionospheric perturbations on the signals. In particular, the GD has allowed us to confirm that the presence of these high-frequency effects in GPS  $L_2$  depends on the type receiver, that is, whether  $L_2$  is acquired with the  $L_1$  aid or not.

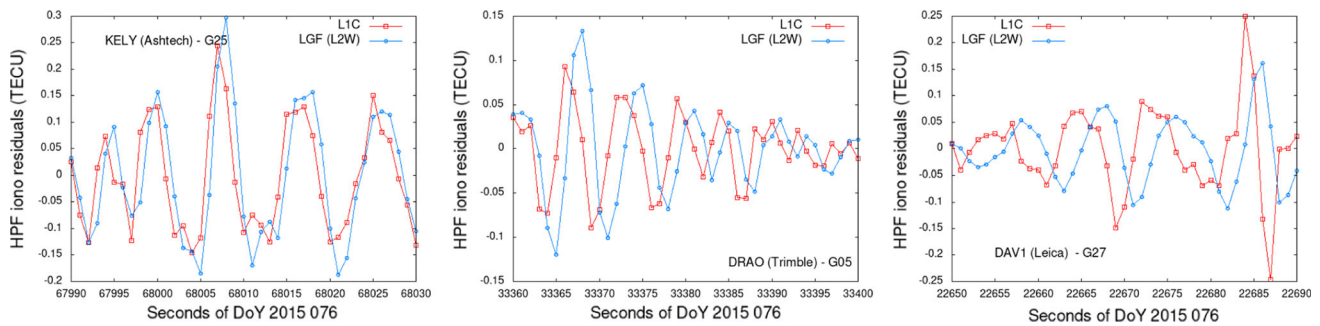


**Fig. 7** Examples showing the delay of the HPF( $L_{GF}$ ) residuals with respect to the  $L_1$  ones from satellite G25 in DoY 76 of 2015, for kely (Ashtech) at left, drao (Trimble) in the middle, and dav1 (Leica) in the right panel

Using the GD approach, we have shown that, for some receivers, the GF combination, which is used to measure high-frequency ionospheric perturbations, heavily underestimate these high-frequency perturbations. Therefore, different receivers could measure different scintillation activity under the same ionospheric event. This is important because many climatological studies about scintillation have been done without considering the receiver types.

Moreover, in some receivers the IF combination, which is typically used for navigation, is far to be free from these high-frequency ionospheric effects. Consequently, some receivers would provide a degraded navigation solution when the solution is obtained under scintillation activity.

We have shown that the use of  $L_1$  to acquire  $L_2$  affects not only the values of the  $L_2$  high-frequency fluctuations, but also introduces a delay in the acquired  $L_2$ . The magnitude of this delay is of few seconds and depends on the receiver type.

Using data stored in RINEX-v3 format, where the signal attributes are specified, for three receiver types, Septentrio, Javad and TPS (Topcon), we have shown that the three receivers acquire L2C signal without the  $L_1$  aid. However, only the Javad receiver seems to acquire L2W without the  $L_1$  aid.

Finally, we have shown that, for data stored in RINEX-v2 format (where  $L_2$  is written without attribute), it is possible to determine whether a specific receiver has acquired  $L_2$  with the  $L_1$  aid. This is important, because old data are stored in RINEX-v2 format. In this sense, we have observed that only Javad receivers acquire L2W without  $L_1$  aid, being the other receivers affected in different magnitude in relation with the technique used to acquire  $L_2$ .

**Acknowledgements** The authors would like to thank International GNSS Service for the availability of precise products and GNSS data.

**Author contributions** JMJ and ARG proposed the general idea of this contribution and initiated the work. JMJ, CCT, and GGC designed and developed the GD tool used in the study. JS and JMJ analysed the results

and wrote the manuscript. ARG, CCT, GGC, JMJ, ROP and JS contributed to the technical discussion and organization of the manuscript. All authors provided advice and critically reviewed the manuscript.

**Funding** Open Access funding provided thanks to the CRUE-CSIC agreement with Springer Nature. The present work was supported by the AEI of Spanish Ministry of Science, Innovation and Universities and European Union FEDER through project RTI2018-094295-B-I00 and by the ESA Contract Number 4000137762/22/NL/GLC/ov.

**Data availability** Precise products (orbits, satellite clocks and troposphere) can be found in the International GNSS Service server <https://gdc.cddis.eosdis.nasa.gov/gps/products/>. GNSS observations can be downloaded from <https://gdc.cddis.eosdis.nasa.gov/gps/data/highrate/>.

**Open Access** This article is licensed under a Creative Commons Attribution 4.0 International License, which permits use, sharing, adaptation, distribution and reproduction in any medium or format, as long as you give appropriate credit to the original author(s) and the source, provide a link to the Creative Commons licence, and indicate if changes were made. The images or other third party material in this article are included in the article's Creative Commons licence, unless indicated otherwise in a credit line to the material. If material is not included in the article's Creative Commons licence and your intended use is not permitted by statutory regulation or exceeds the permitted use, you will need to obtain permission directly from the copyright holder. To view a copy of this licence, visit <http://creativecommons.org/licenses/by/4.0/>.

## References

- Carrano CS, Grooves KM, Rino CI (2019) On the relationship between the rate of change of total electron content index (ROTI), irregularity strength (CkL) and the scintillation index (S4). *J Geophys Res Space Phys* 124:2099–2112. <https://doi.org/10.1029/2018JA026353>
- Cesaroni C, Spogli L, Alfonsi L, De Franceschi G, Ciraolo L, Monaco JFG, Scotto C, Romano V, Aquino M, Bougard B (2015) L-band scintillations and calibrated total electron content gradients over Brazil during the last solar maximum. *J Space Weather Space Clim* 5:A36. <https://doi.org/10.1051/SWSC/2015038>
- Cherniak I, Krankowski A, Zakharenkova I (2018) ROTI maps: a new IGS ionospheric product characterizing the ionospheric irregularities occurrence. *GPS Solut* 22(3):69. <https://doi.org/10.1007/s10291-018-0730-1>

- Correia E, Muella MT, Alfonsi L, dos Santos F, de Oliveira Camargo P (2019) GPS scintillations and total electron content climatology in the Southern American Sector. In: Sanli D (ed) Accuracy of GNSS methods. IntechOpen, London. <https://doi.org/10.5772/intechopen.79218>
- de Oliveira MA, Muella MT, de Paula ER, de Oliveira CB, Terra WP, Perrella WJ, Meibach-Rosa PR (2018) Statistical evaluation of GLONASS amplitude scintillation over low latitudes in the Brazilian territory. *Adv Space Res* 61(7):1776–1789. <https://doi.org/10.1016/j.asr.2017.09.032>
- Guo K, Zhao Y, Liu Y, Wang J, Zhang C, Zhu Y (2017) Study of ionospheric scintillation characteristics in Australia with GNSS during 2011–2015. *Adv Space Res* 59(12):2909–2922. <https://doi.org/10.1016/j.asr.2017.03.007>
- Juan JM, Aragon-Angel A, Sanz J, González-Casado G, Rovira-García A (2017) A method for scintillation characterization using geodetic receivers operating at 1 Hz. *J Geodesy* 91(11):1383–1397. <https://doi.org/10.1007/s00190-017-1031-0>
- Juan JM, Sanz J, Rovira-García A, González-Casado G, Ibáñez D, Orus Perez R (2018a) AATR an ionospheric activity indicator specifically based on GNSS measurements. *J Space Weather Space Clim* 8:A14. <https://doi.org/10.1051/swsc/2017044>
- Juan JM, Sanz J, González-Casado G, Rovira-García A, Camps A, Riba J, Barbosa J, Blanch E, Altadill D, Orus R (2018b) Feasibility of precise navigation in high and low latitude regions under scintillation conditions. *J Space Weather Space Clim* 8:A05. <https://doi.org/10.1051/swsc/2017047>
- Leveson I (2006) Benefits of the new GPS civil signal. *Inside GNSS* 1(5):42–47
- Linty N, Dovis F (2019) An open-loop receiver architecture for monitoring of ionospheric scintillations by means of GNSS signals. *Appl Sci* 9(12):2482. <https://doi.org/10.3390/app9122482>
- Liu Z, Yang Z, Xu D, Morton YJ (2019) On inconsistent ROTI derived from multiconstellation GNSS measurements of globally distributed GNSS receivers for ionospheric irregularities characterization. *Radio Sci.* <https://doi.org/10.1029/2018RS006596>
- McCaffrey AM, Jayachandran PT, Langley RB, Sleewaegen JM (2018) On the accuracy of the GPS L2 observable for ionospheric monitoring. *GPS Solut* 22:23. <https://doi.org/10.1007/s10291-017-0688-4>
- Nguyen VK, Rovira-García A, Juan JM, Sanz J, González-Casado G, La TV, Thung HT (2019) Measuring phase scintillation at different frequencies with conventional GNSS receivers operating at 1 Hz. *J Geodesy* 93(10):1985–2001. <https://doi.org/10.1007/s00190-019-01297-z>
- Pi X, Mannucci A, Lindqwister U, Ho C (1997) Monitoring of global ionospheric irregularities using the worldwide GPS network. *Geophys Res Lett* 24(18):2283–2286
- Rovira-García A, González-Casado G, Juan JM, Sanz J, Orús R (2020) Climatology of high and low latitude scintillation in the last solar cycle by means of the geodetic detrending technique. In: Proceedings of the 2020 international technical meeting of the institute of navigation, San Diego, CA, pp 920–933. <https://doi.org/10.33012/2020.17187>
- Sanz J, Juan JM, Hernández-Pajares M (2013) GNSS data processing, Vol. I: fundamentals and algorithms. ESA Communications, ESTEC TM-23/1, Noordwijk
- Van Dierendonck AJ, Klobuchar J, Hua Q (1993) Ionospheric scintillation monitoring using commercial single frequency C/A code receivers. In: Proceedings of ION GPS 1993, Salt Lake City, Utah, pp 1333–1342
- Woo KT (1999) Optimum semi-codeless carrier phase tracking of L2. In: 12th IONTM, Nashville, Tennessee, September 14–17, 1999
- Yang Z, Liu Z (2016) Observational study of ionospheric irregularities and GPS scintillations associated with the 2012 tropical cyclone Tembin passing Hong Kong. *J Geophys Res Space Phys* 121:4705–4717. <https://doi.org/10.1002/2016JA022398>
- Yang Z, Liu Z (2017) Investigating the inconsistency of ionospheric ROTI indices derived from GPS modernized L2C and legacy L2P(Y) signals at low-latitude regions. *GPS Solut* 21(2):783–796. <https://doi.org/10.1007/s10291-016-0568-3>
- Zakharenkova I, Astafyeva E (2015) Topside ionospheric irregularities as seen from multisatellite observations. *J Geophys Res Space Phys* 120:807–824. <https://doi.org/10.1002/2014JA020330>
- Zhao D, Li W, Li C, Hancock CM, Roberts GW, Wang Q (2022) Analysis on the ionospheric scintillation monitoring performance of ROTI extracted from GNSS observations in high-latitude regions. *Adv Space Res* 69(1):142–158. <https://doi.org/10.1016/j.asr.2021.09.026>